RESEARCH ARTICLE

Ground Servoelasticity Test and Analysis of UAVs With Large Aspect Ratio and Joined-Wing Layout

BI YING [1], **YING ZHUOLIN** [1,2,3,4], **ZHU ZIJIAN** [1,2,3,4], **AND ZHU CHEN** [1,2,3,4]

[1]Institute of Engineering Thermophysics, Chinese Academy of Sciences, Beijing 100190, China
[2]School of Aeronautics and Astronautics, University of Chinese Academy of Sciences, Beijing 100049, China
[3]National Key Laboratory of Science and Technology on Advanced Light-Duty Gas-Turbine, Beijing 100190, China
[4]Key Laboratory of UAV Emergency, Rescue Technology, Ministry of Emergency Management, Beijing 102202, China

Corresponding author: Bi Ying (biying@iet.cn)

ABSTRACT Unmanned aerial vehicles (UAVs) with an ultra-large aspect ratio and a joined-wing configuration exhibit characteristics such as minimal mass, remarkable flexibility, and a unified wing structure, thereby presenting a significant challenge in accurately assessing their dynamic behaviors in terrestrial environments. This study focuses on a specific UAV model characterized by an ultra-large aspect ratio and a joined-wing configuration, which underwent experimental scrutiny under free-free conditions, encompassing the entire aircraft. A rubber rope suspension mechanism was employed to support the UAV, and deliberate efforts were made to eliminate the additional stiffness effect, thus facilitating precise determination of the aircraft's modal characteristics. Subsequent ground-based servoelasticity tests were conducted based on modal experimentation, and specialized filtering techniques were developed to enhance stability. Finally, an analysis of aeroservoelastic stability revealed a strong correlation between simulation and experimental results, with the UAV demonstrating high stability margins in aeroservoelasticity.

INDEX TERMS Ground test, joined-wing, large aspect ratio, servoelasticity.

I. INTRODUCTION

In the past decade, there has been increasing attention towards high-altitude long-endurance (HALE) aircraft, which commonly employ composite materials and super-large aspect ratio configurations. These configurations are characterized by their lightweight structures, low frequencies, and high flexibility. With ongoing design enhancements, the concept of joined-wing layouts has emerged, initially systematically introduced by Wolkovitch in the 1970s [1]. Compared to traditional layouts, joined-wing configurations offer improved wing strength and stiffness, reduced structural weight, and facilitate larger aspect ratio designs to minimize induced drag, enhance maximum lift coefficients, and offer versatile control methods. Additionally, they provide

The associate editor coordinating the review of this manuscript and approving it for publication was Rosario Pecora.

increased space for solar panel installation, garnering global interest [2], [3], [4].

Since the early 21st century, collaborative efforts involving the U.S. Air Force Research Laboratories (AFRL), Boeing, and NASA Langley Research Center have undertaken the SensorCraft project [5], [6], [7], [8], [9], [10], [11] to investigate the aeroservoelastic(ASE) properties of joined-wing aircraft. Kimler and Canfield [12] proposed a control method for pitch motion via wing torsion, along with structural enhancements, demonstrating the efficacy of these approaches through linear, nonlinear static, and flutter analyses. Scott et al. [13] conducted an aeroservoelastic analysis of SensorCraft under transonic conditions, devising gust mitigation control laws that reduced structural dynamics response by 50%. Grauer et al. [14] introduced a novel method for real-time estimation of frequency response and uncertainty, applied to SensorCraft, thereby economizing wind tunnel testing.

This paper focuses on a specific type of UAV with a large aspect ratio joined-wing layout, possessing unique advantages in aerodynamic efficiency and flight performance. However, this configuration introduces novel challenges, particularly in terms of aeroservoelasticity. The coupling of unsteady aerodynamic forces, flight control systems, and aircraft structural dynamics may result in aeroservoelastic instability. To ensure aircraft equipped with servo flight control systems remain stable within their flight envelope, aeroservoelasticity (ASE) analysis is essential. Nonetheless, certain nonlinear elements within servo control systems present challenges in determining their dynamic characteristics accurately via computational methods. Consequently, modal tests and ground servoelasticity tests are necessary prior to aircraft maiden flights [15].

Significant advancements have been made in aeroservoelasticity research in recent years. Liu and Xie [16] considered the geometric nonlinearity of flexible aircraft, linearizing coupling dynamics equations around nonlinear equilibrium states, and conducted aeroservoelastic stability analyses. Zhang et al. [17] performed aeroservoelastic analysis on a large aspect ratio aircraft, employing a linear quadratic Gaussian regulator to actively control the trailing edge, effectively improving flutter boundaries. Huang et al. [18] proposed a modal-based piecewise linear modeling method for nonlinear aeroservoelastic modeling of deformable wings. However, thus far, no scholars have yet conducted ground servoelasticity tests or aeroservoelastic stability studies on ultra-large joined-wing UAVs of this scale. During ground tests of large flexible aircraft, traditional support structures often have relatively high natural frequencies, while the elastic mode frequencies of large flexible aircraft are extremely low. There is a possibility of resonance between the two, which could disrupt the accuracy of the test results. Therefore, appropriate measures must be taken to reduce the support frequencies, ensuring they are significantly lower than the elastic mode frequencies of the aircraft, in order to guarantee the effectiveness and accuracy of ground tests.

This paper conducts aeroservoelastic analysis and ground servoelasticity tests for a specific type of ultra-large aspect ratio joined-wing UAV. Stiffness corrections are applied during calculations using a rubber rope suspension support method to obtain accurate dynamic responses. Building upon this, a set of ground servoelasticity test methods suitable for ultra-large aspect ratio joined-wing UAVs is established, providing reliable data support for subsequent aeroservoelastic analyses.

The organization of this paper is as follows: Section II introduces the theoretical background of ground servoelasticity testing principles, detailing the method of stiffness correction for the suspension system. Section III describes the state of combined wing aircraft, sensor arrangements, and discusses suspension system stiffness effects and their corrections. Ground servoelasticity testing and filter design are outlined in Section IV. Section V conducts aeroservoelastic simulation calculations and comparative analyses based on

test results. Finally, Section VI highlights several concluding observations.

II. THEORETICAL BACKGROUND
A. BASIC PRINCIPLES OF THE TEST
Ground servoelasticity tests encompass open-loop frequency response and closed-loop impulse response tests. The open-loop frequency response test evaluates the transfer characteristics of aircraft structures and flight control systems, aiming to establish accurate mathematical models for aeroservoelastic analysis. The closed-loop stability test examines the stability and stability margins of the closed-loop coupling system formed by the aircraft structure and flight control system to ensure sufficient servoelastic stability [19].

The schematic diagram of the test is depicted in Figure 1, where the red line represents analog signals and the blue line indicates digital signals.

For the open-loop frequency response test, the control law of a specific channel of the flight control system is either disconnected or connected, and a sinusoidal excitation signal is applied to the input of the servo command test. Output signals from each measurement port are collected, while simultaneously monitoring the vibration of the aircraft structure. Through data processing, the open-loop transfer function of the servoelastic system is derived. The stability margin is determined according to the Nyquist criterion in classical control theory, and the stability margin is assessed.

In the closed-loop impulse response test, the control laws of all channels of the flight control system are activated, and a pulse excitation signal is applied to the input of the servo command test. Output signals from each measurement port are collected, while simultaneously monitoring the vibration of the aircraft structure. The test considers different multiples of the control law gain to verify the stability and stability margin of the coupling between the structure and the flight control system.
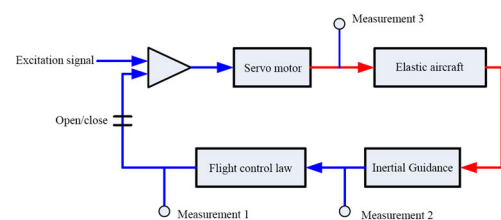

FIGURE 1. Ground servoelasticity test schematic.

As the test object, the UAV collects excitation signals, rudder actuator output signals, output signals from the inertial navigation components, and output signals from the flight control laws via the onboard flight control computer. This data is then transmitted bidirectionally with the portable data acquisition system through the serial port. The vibration accelerometer monitoring signals at key positions of the test object are directly transmitted to the portable data acquisition system via cable. The test computer is connected to the portable data acquisition system via cable, using Ethernet

communication to transmit test measurement data to the test computer for data processing and analysis. Simultaneously, the test statuses, including channel switch modal words, control surface control modes, excitation signals, and channel gain multiples, are transmitted to the flight control computer.

B. DATA PROCESSING METHODS

The open-loop frequency response test is conducted using a stepwise sinusoidal signal for excitation. The characteristic of this signal is as follows: within the selected frequency range, sinusoidal signals of equal amplitude are successively emitted at incremental steps from low to high frequencies, and each frequency point is maintained for a certain period of time.

At the i frequency point ω_i, the excitation signal $x_i(t)$ and the response signal $y_i(t)$ are captured, where $T_1 < t < T_2$. To eliminate the steady-state component from the response signal, the signal $y_i(t)$ is first zero-meaned. Assuming there are n sampling points, i.e., $y_i(t_1), y_i(t_2), \cdots, y_i(t_1)$, the following processing is carried out:

$$\bar{y}_i(t_j) = y_i(t_j) - \frac{1}{n} \sum_{k=1}^{n} y_i(t_k) \tag{1}$$

Since the excitation signal is a given sinusoidal function, i.e.,

$$x_i(t) = a \sin(\omega_i t) \tag{2}$$

According to the principle of linear systems, the system output is also a sinusoidal function, i.e.,

$$\bar{y}_i(t) = A_i a \sin(\omega_i t + \phi_i) \tag{3}$$

Expanding the above equation, it simplifies to:

$$\bar{y}_i(t) = A_i \cos \phi_i \cdot a \sin \omega_i t + A_i \sin \phi_i \cdot a \cos \omega_i t \tag{4}$$

For n sampling points, the above equation can be written as:

$$\begin{bmatrix} a \sin \omega_i t_1 & a \cos \omega_i t_1 \\ a \sin \omega_i t_2 & a \cos \omega_i t_2 \\ \vdots & \vdots \\ a \sin \omega_i t_n & a \cos \omega_i t_n \end{bmatrix} \begin{bmatrix} A_i \cos \phi_i \\ A_i \sin \phi_i \end{bmatrix} = \begin{bmatrix} \bar{y}_i(t_1) \\ \bar{y}_i(t_2) \\ \vdots \\ \bar{y}_i(t_n) \end{bmatrix} \tag{5}$$

This equation is overdetermined, and it can be expressed in the following form:

$$\mathbf{Ku = f} \tag{6}$$

Using the least squares method to solve the overdetermined equation, we obtain:

$$\mathbf{u} = \left(\mathbf{K}^T \mathbf{K} \right)^{-1} \mathbf{K}^T \mathbf{f} \tag{7}$$

From this, the frequency response function corresponding to the frequency is:

$$G(j\omega_i) = u_1 + ju_2 = A_i \cos \phi_i + jA_i \sin \phi_i \tag{8}$$

Here, A_i and ϕ_i are the magnitude and phase of the frequency response function at frequency ω_i.

This method can avoid the problem of missing sinusoidal peaks during sampling and has a certain noise reduction effect when using the least squares method to solve for the amplitude and phase of the frequency response function.

The closed-loop coupled system composed of the structure and flight control system can be represented by Figure 2. The open-loop transfer function of the system is:

$$L_{open} = -K(s)G(s) \tag{9}$$

When the control loop is disconnected (i.e., $E(s) = R(s)$), we have:

$$L_{open} = -\frac{Y(s)}{E(s)} = -\frac{Y(s)}{R(s)} \tag{10}$$

When the control loop is closed (i.e., $E(s) = R(s) - Y(s)$), we have:

$$\frac{Y(s)}{R(s)} = -\frac{K(s)G(s)}{1 - K(s)G(s)} \tag{11}$$

When $|K(s)G(s)| \ll 1$, the following approximation can be made:

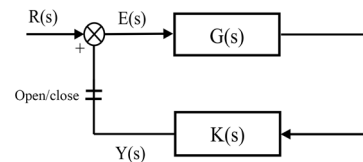$$L_{open} = -K(s)G(s) = -\frac{Y(s)}{E(s)} \approx -\frac{Y(s)}{R(s)} \tag{12}$$

FIGURE 2. Example of stepwise sinusoidal excitation signal and its response.

C. MODIFICATION OF ADDITIONAL STIFFNESS OF THE SUSPENSION SYSTEM

The hanging method, characterized by its simple structure and low cost, is often employed to simulate the free-free boundary conditions required for ground tests of structures [20]. Due to the influence of additional stiffness from the suspension system, there exists a deviation between the directly measured first symmetric bending mode of the front wing and the actual modal characteristics of the aircraft. During the testing process, the influence of the suspension system stiffness was addressed using I-deas modal testing software. The specific principles are as follows:

Considering the general case of a multi-point rigid constraint equation, the total energy in the system can be represented as

$$\frac{1}{2} \left(\chi^t H^{-1} \chi \right) - \chi^t F$$

where χ represents the structural response vector, F represents the force vector, and H represents the transfer function matrix.

The constraint equations can be represented as

$$C^t \chi = 0 \tag{13}$$

where C represents the constraint coefficient matrix.

The response of the structure can be obtained by finding the extremum of the total energy of the system under the constraints of the equations, which is equivalent to finding an equilibrium point of a constrained quadratic functional.

$$\left[\begin{array}{c} \frac{1}{2} \left(\chi^t H^{-1} \chi \right) - \chi^t F \\ C^t \chi = 0 \end{array} \right] \tag{14}$$

By incorporating the Lagrange multipliers into Equation (14), then the problem becomes equivalent to solving the following system of linear equations

$$\left[\begin{array}{cc} H^{-1} & C \\ C^t & 0 \end{array} \right] \left[\begin{array}{c} \chi \\ \gamma \end{array} \right] = \left[\begin{array}{c} F \\ 0 \end{array} \right] \tag{15}$$

From Equation (15), it can be seen that the response of the structure can be expressed as

$$\chi = HF - HC\gamma \tag{16}$$

Multiplying Equation (16) by the transpose of the constraint matrix yields, to get

$$C^t \chi = C^t HF - C^t HC\gamma = 0 \tag{17}$$

In that case, the response of the structure under constraints is

$$\chi = \left(1 - HC \left(C^t HC \right)^{-1} C^t \right) HF \tag{18}$$

This general formula is applicable to rigidly connecting two points, forcing the two points to move parallel to each other or in parallel within a certain plane, as well as enforcing transmission ratios in torsional systems.

The poles of the modified system can be solved from the homogeneous solution of Equation (17),

$$C^t HC\gamma = 0 \tag{19}$$

Based on the poles of the modified system, the proportional residues that constitute the modal shapes of the corrected system can be obtained from Equation (18).

The method of connecting two points can be used to connect individual components. Therefore, the analytical transfer functions of connectors (e.g., springs, mass dampers, and buffers) can be provided, and structural corrections can be made by providing appropriate rigid constraints for the superimposed transfer function matrix. The superimposed transfer function matrix can be expressed as

$$H = \left[\begin{array}{cccccc} H_0 & 0 & 0 & 0 & \ldots & 0 \\ 0 & H_1 & 0 & 0 & \ldots & 0 \\ 0 & 0 & H_2 & 0 & \ldots & 0 \\ 0 & 0 & 0 & H_3 & \ldots & 0 \\ \ldots & \ldots & \ldots & \ldots & \ldots & 0 \\ 0 & 0 & 0 & 0 & 0 & H_n \end{array} \right] \tag{20}$$

where H0 is the transfer function matrix of the original system, H_1 is the transfer function matrix of system 1, H_2 is the transfer function matrix of system 2, H_3 is the transfer function matrix of system 3, and H_n is the transfer function matrix of system n.

In general, structural modifications can be made using substructures, mass cancellations, or response ratios, including rigid connections, flexible connections, concentrated masses, spring-mass dampers, two-degree-of-freedom rigid connectors, and two-degree-of-freedom flexible connectors.

In this formula, all modifications are applied as rigid constraints. Modifications involving connectors can be further decomposed by treating the connectors as separate subsystems, which allows for greater flexibility. For example, considering the original system and a connector, Equation (19) can be written as

$$\left[C_0^t H_0 C_0 + C_1^t H_1 C_1 \right] \gamma = 0 \tag{21}$$

where C_0 represents the part of the constraint matrix that belongs to the original system, and C_1 is the part of the constraint matrix that belongs to the connector or system 1.

Additionally, the transfer function matrix of one or all subsystems can be represented by the eigenvalues and eigenvectors of the atomic system as follows

$$H = \psi \left[a \left(s - p \right) \right]^{-1} \psi^t \tag{22}$$

where ψ represents the eigenvector of the original system, a represents the mode, s represents the Laplace variable, and p represents the eigenvalue or pole of the atomic system.

III. SYSTEM DEVELOPMENT

A. MODEL DESCRIPTION: A UAV WITH ULTRA-LARGE ASPECT RATIO AND JOINED-WING LAYOUT

Figure 3 illustrates a research UAV characterized by an ultra-large aspect ratio and a joined-wing layout. The test model encompasses the airframe structural system, control system, onboard equipment, energy system, and power system. The diamond-wing joined-wing configuration aircraft boasts an approximate wingspan of 60m and a fuselage length of approximately 35m. The main wings are segmented into front wings, aft wings, and outboard wings. Two joints interconnect the front wing and outboard wing, subsequently linking them to the aft wing.

The mass characteristic parameters of the entire aircraft are outlined in Table 1, while the coordinate system for this UAV is established as depicted in Figure 4. The head point of the payload bay serves as the coordinate origin, with the aircraft's nose pointing towards the tail representing the positive direction of the X-axis. The Y-axis is perpendicular to the plane of symmetry of the aircraft, with the positive direction towards the right of the pilot. Additionally, the Z-axis adheres to the right-hand rule, with the positive direction pointing upwards.

To simulate the free-free state of the test aircraft, the experiment used a rubber cord suspension support. Specifically, a 5-point suspension method was used to horizontally suspend the aircraft. The upper ends of the rubber cords were fixed to a crane using a manual hoist, and the lower ends were installed at various suspension points of the aircraft through force sensors. When lifted, the landing gear tires were 0.1m above the ground to prevent accidental drops from causing damage to the product, and a protective cradle was used underneath

TABLE 1. The mass characteristic parameters of the entire aircraft.

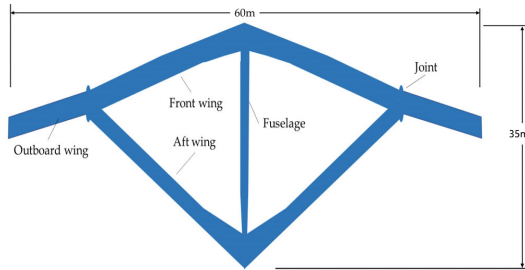| Parameters	X (mm)	Y (mm)	Z (mm)
Center of Gravity	14000	0	1500
Moment of Inertia for Model (Using Center of Gravity as Center).	I_{XX} (kg·m^2)	I_{YY} (kg·m^2)	I_{ZZ} (kg·m^2)
	231600.0	45660.0	287400.0
	I_{XY} (kg·m^2)	I_{YZ} (kg·m^2)	I_{XZ} (kg·m^2)
	0.0	0.0	-8010.0
Mass	1500kg		

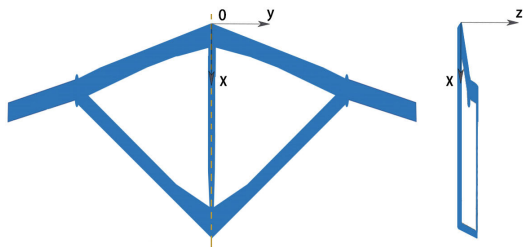**FIGURE 3.** A schematic diagram of the structure.

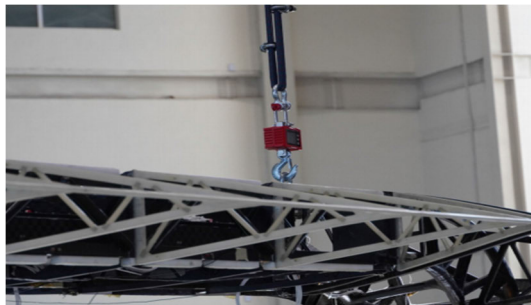**FIGURE 4.** The coordinate definition diagram.

FIGURE 5. Installation diagram of the left side panel suspension point.

TABLE 2. Coordinates of the suspension point.

Location of the Suspension Point	X (mm)	Y (mm)	Z (mm)
Right Front Suspension Point	1200	1200	300
Left Front Suspension Point	1200	-1200	300
Right Side Panel Suspension Point	15000	20000	3000
Left Side Panel Suspension Point	15000	-20000	3000
Tail Suspension Point	30500	0.0	3500

the aircraft for safety protection. The coordinates of the suspension points are shown in Table 2, the installation of rubber cords at each suspension point is provided in Table 3, and the suspension effects of the aircraft suspension points are illustrated in Figure 5 and Figure 6.

TABLE 3. The installation of rubber cords at each suspension point.

Location of the Suspension Point	Diameter (mm)	Length (m)	Number
Right Front Suspension Point	20	9	3
Left Front Suspension Point	20	9	3
Right Side Panel Suspension Point	16	7.5	4
Left Side Panel Suspension Point	16	7.5	4
Tail Suspension Point	20	8	3

TABLE 4. Suspension system frequencies.

Rigid Motion	Suspension System Frequency /Hz
X-axis Translation	———
Y-axis Translation	———
Z-axis Translation	0.28
X-axis Rotation	0.24
Y-axis Rotation	0.44
Z-axis Rotation	0.01

FIGURE 6. Installation diagram of the right side panel suspension point.

TABLE 5. The stiffness of rubber cords at each suspension point.

Location of the Suspension Point	Right Front	Left Front	Right Side Panel	Left Side Panel	Tail
Rubber Cord Stiffness (N/m)	1088	1050	752	752	1458
ID Number of the measurement point where the negative stiffness is applied	40	116	137	251	318

According to the field measurements, the frequency of the rigid body movement of the aircraft with the support of rubber rope is shown in Table 4.

Based on the modal test results of the experimental aircraft, it was found that the maximum support frequency of the aircraft is lower than one-third of the frequencies of all modes except the first three elastic modes. However, due to height restrictions at the test site, the rubber ropes cannot be sufficiently long to decrease the frequency of the suspension system. Therefore, in Section B, an assessment was conducted to mitigate the impact of the suspension system stiffness on the frequencies of the first three elastic modes.

B. IMPACT ANALYSIS AND MODIFICATION OF THE SUSPENSION AND TESTING SYSTEMS

Due to the fact that the support frequency of the rubber cord suspension system exceeds one-third of the first two orders of modal frequency, it is necessary to correct the impact brought

TABLE 6. Comparison of modal frequencies before and after modification.

Test State	Modal Name	1st	2nd	3rd	4th	5th	6th
	Test Frequency (Hz)	0.605	1.024	1.452	1.580	2.285	3.846
Before the Equipment Removal	Frequency after deducting support system stiffness (Hz)	0.481	1.026	1.445	1.574	2.279	3.840
	Deviation (%)	-20.566	0.195	-0.482	-0.380	-0.263	-0.156
	Test Frequency (Hz)	0.625	1.033	1.474	1.621	2.294	3.889
After the Equipment Removal	Frequency after deducting support system stiffness (Hz)	0.497	1.036	1.468	1.613	2.285	3.883
	Deviation (%)	-20.484	0.290	-0.407	-0.494	-0.392	-0.154

TABLE 7. Modal summary table.

Modal Order	Modal Description	Frequency (Hz)	Indicator Function	Damping Coefficient
1	Front wing first symmetric bending	0.447	0.902	0.012
2	Front wing first anti-symmetric bending	1.031	0.931	0.009
3	Aft wing first anti-symmetric bending	1.139	0.966	0.007
4	Front wing first symmetrical torsion	1.473	0.976	0.010
5	Aft wing first symmetric bending	1.594	0.967	0.011
6	Front wing first anti-symmetrical torsion	1.679	0.945	0.008
7	Front wing second symmetric bending	2.305	0.973	0.023
8	Front wing first anti-symmetric in-plane bending	3.159	0.903	0.007
9	Aft wing second symmetric bending	3.405	0.900	0.009
10	Front wing second anti-symmetric bending	3.567	0.934	0.009
11	Aft wing first symmetric in-plane bending	3.859	0.970	0.017
12	Vertical tail first bending	4.226	0.977	0.018
13	Front wing first symmetric in-plane bending	4.427	0.926	0.018
14	Flap first symmetrical in-plane bending	4.641	0.956	0.015
15	Flap first anti-symmetrical in-plane bending	4.746	0.867	0.023

by the stiffness of the suspension system. This modification specifically selected the first six orders of elastic mode for adjustment, and the principle of the modification method used on the test site is described in Chapter II, Section II-C.

During the test, the frequency response function curve of the body is obtained by testing with the phase separation method, and the frequencies and mode shapes of the main mode are identified. Then, the test model could be calculated using the frequency response function, and the frequencies and mode shapes of the main modes. Subsequently, negative stiffness was applied vertically at measurement points near the suspension points to deduct the additional stiffness of each suspension point in the test model. Since the stiffness of the rubber cord would be affected by the amount of deformation, we obtained the curve of the rubber cord stiffness changing with load by applying force to the cord section before the test.

During the test, the actual stiffness of the rubber cord in the suspended state was measured by reading the values of the force sensors attached to the cord section, with specific values shown in Table 5.

In order to avoid the deviation caused by the modifications of the single test results, tests were conducted both in the test state and the state of removing the mass of the equipment installed on the outboard wings. Then, the effect due to the additional stiffness of the support system is corrected for both states according to the test results obtained by the phase separation method, and the modal frequencies before and after the modifications are shown in Table 6.

It can be seen that the results of the additional stiffness modification are essentially consistent under two conditions. The impact of the suspension system's additional stiffness on

the frequency of the front wing first symmetric bending is approximately 20.566%, while the influence on other elastic modal frequencies is less than 0.5%. Therefore, it is only necessary to correct the frequency of the front wing first symmetric bending.

To eliminate the effects of nonlinear factors, the frequency measured by the phase resonance method is taken as the test result affected by the stiffness of the support system. By making modifications based on the same proportion of influence on the basis of 0.563Hz, the frequency of the front wing first symmetric bending can be obtained as 0.447Hz.

Similarly, the impact of additional mass due to sensors and test cables was also analyzed. During the test, a total of 360 accelerometers were attached, each weighing less than 5g, and 360 test cables were connected, with the total mass is approximately 3g. The additional mass brought by the accelerometers and cables was about 3.88 kg, which was evenly distributed across all measurement points. The effect of the additional mass on the test results frequency was less than 0.1%, and such a minor impact could be ignored.

C. MODAL TEST RESULTS AFTER STIFFNESS MODIFICATION

In order to preliminarily determine the frequency distribution of the entire aircraft within the frequency band of interest, various excitation force configurations were first used within the frequency band of the required modes to perform multi-point step sine sweep tests. This resulted in the FRF (frequency response function) curve of the system, and the resonance peaks that appeared were identified and separated one by

one. At a certain peak frequency, by adjusting the force and frequency to make $C(f_r) \rightarrow 1$, it can be considered that the aircraft is vibrating in the r-th order single mode (i.e., pure mode), while its vibration frequency is the r-th order natural frequency of the aircraft, and the vibration mode of the entire aircraft at this time is the r-th order natural mode shape of the aircraft. After the identification of each mode is completed, the damping coefficient for that order mode is calculated using the half-power method according to the amplitude-frequency curve. This test only studies the key modes of the entire aircraft, including the front wing, fuselage, aft wing, and vertical tail. The results of the pure modal tests are shown in Table 7, and it can be seen that the indicator function values for each order mode are all greater than 0.9, indicating a high modal purity.

D. CONTROL LAW STATES

The control law for longitudinal pitch attitude maintenance is

$$\eta_y = K_\theta (\theta - \theta_c) + K_{\theta i} \int (\theta - \theta_c)\mathrm{d}t + K_q q \quad (23)$$

wherein, η_y is the elevator deflection angle command, θ is the pitch angle, q is the pitch angle velocity, and the parameters in the formula are shown in Table 8.

TABLE 8. Parameters of longitudinal control law.

Altitude(m)	K_θ	$K_{\theta i}$	K_q
5	6	0.02	0.05
1500	6	0.02	0.05
5000	4	0.02	0.05
10000	3	0.02	0.05
15000	3	0.02	0.5
20000	2	0.02	0.1

In the actual test, the low-pass filtering of the pitch angular velocity signal is carried out in some test states, the first-order inertial filtering with a cut-off frequency of 2Hz is adopted, and the bilinear transformation is adopted under the 40ms duty cycle of the flight control system, and the filter structure of the continuous and discrete systems is as follows

$$G_{LPF}(s) = \frac{12.5664}{s + 12.5664}$$

$$G_{LPF}(z^{-1}) = \frac{0.2008 + 0.2008z^{-1}}{1 - 0.5983z^{-1}} \quad (24)$$

The control law for lateral heading inner loop (roll attitude hold BTT) is

$$\eta_x = K_\phi (\phi - \phi_c) + K_{\phi i} \int (\phi - \phi_c)\mathrm{d}t + K_p p + K_{z2x} \frac{r}{s+1}$$

$$\eta_z = K_r \frac{r}{s+1} \quad (25)$$

where, η_x and η_z respectively represent the aileron deflection angle command and the rudder deflection angle command, p and r respectively represent the roll rate and yaw rate, ϕ represents the roll angle, and the gain parameters for each are shown in Table 9.

TABLE 9. Parameters of lateral heading control law.

Altitude(m)	K_ϕ	$K_{\phi i}$	K_p	K_{z2x}	K_r
5	15	0.5	0.1	9	4
1500	15	0.5	0.1	9	4
5000	10	1	0.2	9	4
10000	10	1	0.2	9	4
15000	6	0.5	0.2	9	4
20000	3	0.5	1	9	6

The control law for lateral heading inner loop (roll attitude hold STT) is

$$\eta_x = K_\phi \phi + K_p p$$

$$\eta_z = K_r \frac{r}{s+1} \quad (26)$$

where, η_x and η_z respectively represent the aileron deflection angle command and the rudder deflection angle command, p and r respectively represent the roll rate and yaw rate, and ϕ represents the roll angle. The gain parameters are fixed values, specified as follows:

$$K_\phi = 13, \quad K_p = 3, \quad K_r = 0.24$$

In practical experiments, a low-pass filter is applied to the roll rate signal for certain test conditions. A first-order inertial filter with a cutoff frequency of 2Hz is employed. Considering a flight control system with a 40ms operating cycle, the continuous-to-discrete filter structure is obtained using the bilinear transform and is as follows:

$$G_{LPF}(s) = \frac{12.5664}{s + 12.5664}$$

$$G_{LPF}(z^{-1}) = \frac{0.2008 + 0.2008z^{-1}}{1 - 0.5983z^{-1}} \quad (27)$$

The UAV control scheme for this test is divided into two types: "longitudinal pitch attitude hold-transverse heading roll attitude hold BTT" and "longitudinal pitch attitude hold-transverse heading roll attitude hold STT". Meanwhile, due to variations in control parameters with indicated airspeed and altitude, nodes with relatively high control gains for indicated airspeed and altitude are selected for the test. The specific states of the control laws are detailed in Table 10.

TABLE 10. Control law status.

No.	Control Scheme	Altitude (m)	Indicated Airspeed (m/s)
1	BTT	1500	9.04
2	BTT	15000	9.04
3	BTT	20000	9.04
4	STT	1500	9.04

IV. GROUND SERVOELASTICITY TEST
A. OPEN-LOOP FREQUENCY RESPONSE TEST
In the longitudinal open-loop test, there are three sets of test items corresponding to different control parameters. The project numbers and parameters are listed in Table 11.

TABLE 11. Items and parameters of longitudinal open-loop test.

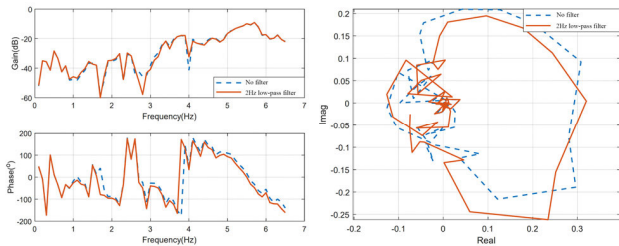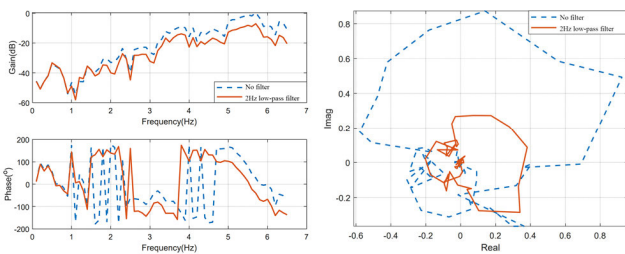| No.	Control Scheme	Altitude(m)	Control Gain
KA01	BTT	1500	1.0
KA02	BTT	15000	1.0
KA03	STT	1500	1.0

FIGURE 7. Comparison of open-loop frequency response function for Pitch Channel KA01.

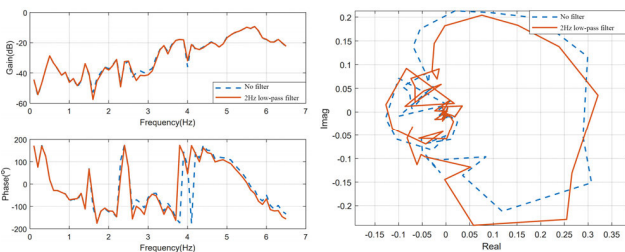**FIGURE 8.** Comparison of Open-loop Frequency Response Function for Pitch Channel KA02.

FIGURE 9. Comparison of Open-loop Frequency Response Function for Pitch Channel KA03.

All three sets of test states for the listed longitudinal channels are excited by step sinusoidal signals, with frequencies ranging from 0.1 to 6.5 Hz and signal amplitudes of 2 degrees. It is important to note that the global margin corresponds to the maximum amplitude point in the amplitude-frequency curve, which does not characterize the system's stability. For the stability analysis of the system after adding a 2Hz low-pass filter, considering that the frequency response characteristics of the angle and angular velocity loops have been obtained in the open-loop frequency response test without a filter, only a discrete 2Hz low-pass filter is added during data processing. The open-loop frequency response function of the system after considering the filter is then calculated for stability analysis. The resulting open-loop frequency response function curve after adding the filter is shown in Figure 7 to Figure 9.

TABLE 12. The stability results of open-loop frequency response test (longitudinal channel).

No.	Filter	Amplitude Margin(dB)	Phase Margin (Deg)	Gain Margin (dB)	Stability
KA01	No Filter	18.24(3.8Hz)	——	9.08(5.7Hz)	Stable
	2Hz Low-pass Filter for Pitch Rate	18.34(3.8Hz)	——	9.09(5.7Hz)	Stable
KA02	No Filter	11.18(4.6Hz)	——	-0.40(5.7Hz)	Stable
	2Hz Low-pass Filter for Pitch Rate	17.95(3.8Hz)	——	8.97(5.7Hz)	Stable
KA03	No Filter	18.20(3.8Hz)	——	9.30(5.7Hz)	Stable
	2Hz Low-pass Filter for Pitch Rate	18.22(3.8Hz)	——	9.30(5.7Hz)	Stable

TABLE 13. Results of longitudinal modal tests.

No.	Modal Name	Modal Frequency (Hz)
1	Front Wing Symmetric Bending	0.56
2	Front Wing Symmetric Torsion	1.47
3	Rear Wing Symmetric Bending	1.59
4	Outer Power Bay Symmetric Pitch	2.22
5	Front Wing Symmetric Second Bending	2.31
6	Mid Power Bay Symmetric Pitch	2.48
7	Inner Power Bay Symmetric Pitch	2.62
8	Rear Wing Symmetric Second Bending	3.41
9	Inner Wing Face Symmetric Bending	4.43
10	Small Wing Face Symmetric Bending	4.64
11	Outer Wing Symmetric Torsion	5.18
12	Fuselage Vertical Bending	5.68

Table 12 presents the stability results of the three test groups. From the amplitude margins, it can be observed that the servoelastic systems are stable, meeting the specification requirements of amplitude margins greater than 6dB and phase margins greater than 45°. Among these, KA01 and KA03 represent the 1500-meter low-altitude states of the BTT and STT control schemes, respectively. With identical control parameters, excluding considerations for coupling in the other two channels, these two sets of test states are deemed consistent. Given the pitch rate control gain of 0.05 for both sets, the primary contributor to servoelastic system stability is the pitch angle loop. Thus, the impact of adding a 2Hz low-pass filter to the system's stability after including pitch rate is minimal. KA02 corresponds to the BTT control scheme at 15,000 feet altitude, with the highest pitch rate control gain, resulting in the smallest amplitude margin. The system's amplitude margin significantly improves after adding the 2Hz low-pass filter. In all three test groups, the open-loop frequency response function curves without filters are situated near the longitudinal correlation modes, with the relevant mode test results listed in Table 13.

There are 5 groups of test items according to different control parameters, and the project numbers and parameters are listed in Table 14. Among these, KB04, and 05 are the open-loop tests in the transverse heading coupling state (aileron open-loop, rudder closed-loop) to investigate the influence of the heading channel on the transverse open-loop transmission characteristics.

TABLE 14. Items and parameters of lateral open-loop test.

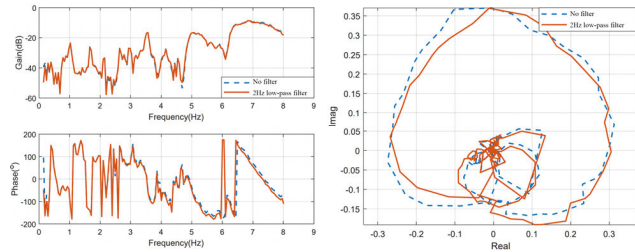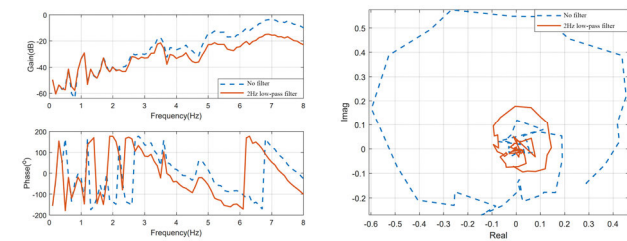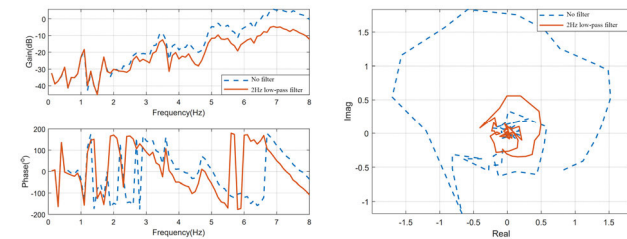| No.	Control Scheme	Altitude(m)	Control Gain
KB01	BTT	1500	1.0
KB02	BTT	15000	1.0
KB03	STT	1500	1.0
KB04	BTT	1500	1.0
KB05	STT	1500	1.0

FIGURE 10. Comparison of Open-loop Frequency Response Function for Roll Channel KB01.

FIGURE 11. Comparison of Open-loop Frequency Response Function for Roll Channel KB02.

FIGURE 12. Comparison of Open-loop Frequency Response Function for Roll Channel KB03.
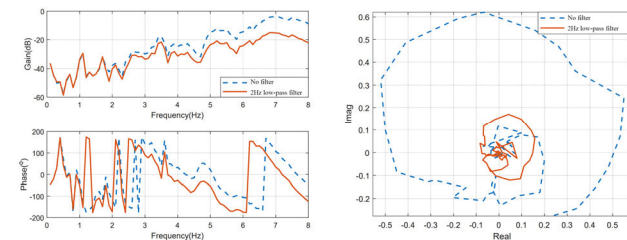

FIGURE 13. Comparison of Open-loop Frequency Response Function for Roll Channel KB04.

The 5 groups of test states for the lateral channels listed are all excited by stepping sinusoidal signals, with frequencies ranging from 0.1 to 8.0 Hz, and signal amplitudes of 2 degrees. Similar to the pitch channel, the roll angle velocity
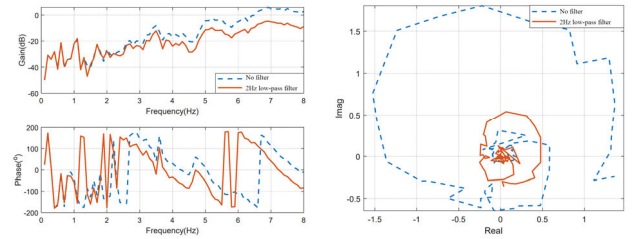

FIGURE 14. Comparison of Open-loop Frequency Response Function for Roll Channel KB05.

TABLE 15. Open-loop frequency response test stability results (lateral channel).

No.	Filter	Amplitude Margin (dB)	Phase Margin (Deg)	Gain Margin (dB)	Stability
KB01	No Filter	11.37 (6.5Hz)	——	8.39 (6.8Hz)	Stable
	2Hz Low-pass Filter for Roll Rate	11.07 (6.4Hz)	——	7.50 (6.8Hz)	Stable
KB02	No Filter	5.61 (6.7Hz)	——	3.70 (6.9Hz)	Stable (Low Margin)
	2Hz Low-pass Filter for Roll Rate	21.45 (6.1Hz)	——	14.76 (6.9Hz)	Stable
KB03	No Filter	-1.47 (6.7Hz)	——	-5.78 (6.9Hz)	Unstable
	2Hz Low-pass Filter for Roll Rate	11.65 (6.1Hz)	——	4.45 (6.9Hz)	Stable
KB04	No Filter	6.51 (6.6Hz)	——	3.93 (6.9Hz)	Stable
	2Hz Low-pass Filter for Roll Rate	22.47 (6.1Hz)	——	15.00 (6.9Hz)	Stable
KB05	No Filter	-2.75 (6.6Hz)	——	-5.80 (6.9Hz)	Unstable
	2Hz Low-pass Filter for Roll Rate	14.07 (6.0Hz)	——	4.71 (6.9Hz)	Stable

TABLE 16. Lateral correlated modal test results.

No.	Modal Name	Modal Frequency (Hz)
1	Front Wing Symmetric Bending	0.56
2	Front Wing Symmetric Torsion	1.47
3	Rear Wing Symmetric Bending	1.59
4	Outer Power Bay Symmetric Pitch	2.22
5	Front Wing Symmetric Second Bending	2.31
6	Mid Power Bay Symmetric Pitch	2.48
7	Inner Power Bay Symmetric Pitch	2.62
8	Rear Wing Symmetric Second Bending	3.41
9	Inner Wing Face Symmetric Bending	4.43
10	Small Wing Face Symmetric Bending	4.64
11	Outer Wing Symmetric Torsion	5.18
12	Fuselage Vertical Bending	5.68

with a 2 Hz low-pass filter (see Section C) is calculated by adding a discrete 2 Hz low-pass filter to the unfiltered state test data. The stability results of the open-loop frequency response test are listed in Table 15, and the curve of the open-loop frequency response function after adding the filter is shown in Figure 10 to Figure 14.

TABLE 17. Items and parameters of heading open-loop test.

No.	Control Scheme	Altitude(m)	Control Gain
KC01	BTT	1500	1.0
KC02	BTT	20000	1.0
KC03	STT	1500	1.0
KC04	BTT	1500	1.0
KC05	STT	1500	1.0

TABLE 18. Open-loop frequency response test stability results (Yaw channel).

No.	Amplitude Margin (dB)	Phase Margin (Deg)	Overall Margin (dB)	Stability
KC01	44.94	——	38.90	Stable
KC02	43.37	——	34.47	Stable
KC03	>60	——	>60	Stable
KC04	48.08	——	37.68	Stable
KC05	44.34	——	34.38	Stable

From the open-loop test results listed in Table 15, KB01 corresponds to the 1500-meter low-altitude state of the BTT control scheme, meets the specification requirements of amplitude margins greater than 6dB and phase margins greater than 45°. The roll angle velocity control gain is only 0.1, the roll angle loop has a great influence on the stability of the servoelastic system, so after adding the roll angle speed 2Hz low-pass filter, the stability margin of the system changes very little; KB02 corresponds to the 20000-meter high-altitude state of the BTT control scheme, the stability margin is low, KB03 corresponds to the 1500-meter low-altitude state of the STT control scheme, the servoelastic system is unstable, and the stability margin of the system is greatly improved after adding the 2Hz low-pass filter of the roll angle speed; KB04 and KB05 is the transverse and lateral coupling state corresponding to KB01 and KB03, and it can be seen from the stability margin results that the heading channel has little influence on the stability of the transverse channel, and the transverse heading coupling effect is weak. The peaks of the amplitude-frequency curve are located near the transverse correlation modes, and the test results of the correlation modes are listed in Table 16.

There are 5 groups of test items according to the different control parameters, and the project numbers and parameters are listed in Table 17, among which KC04 and 06 are the open-loop tests in the transverse heading coupling state, investigating the influence of the transverse channel on the open-loop transmission characteristics of the course.

The 5 groups of test states of the listed heading channels are all excited by stepping sinusoidal signal, with a frequency range from 0.1 to 8.0Hz, and a signal amplitude of 2 degrees. The stability results of the open-loop frequency response test are listed in Table 18. It can be seen from the test results that all states of the heading channel are stable, with a stability margin not less than 40dB, meeting the specification requirements of amplitude margin greater than 6dB and phase margin greater than 45°.

TABLE 19. Items and parameters of longitudinal closed-loop test.

No.	Control Scheme	Altitude(m)	Control Gain
BA01	BTT	1500	K
BA02	BTT	15000	K
BA03	STT	1500	K

TABLE 20. Closed-loop impulse response test results (Longitudinal channel).

No.	Filter	Control Gain	Stability
BA01	No Filter	5.0x	Stable
		6.5x	Stable
		8.0x(18.06dB)	Stable (18.06dB)
BA02	No Filter	1.0x	Stable
		2.0x	Stable
		2.5x(7.96dB)	Unstable (Critical state, instability frequencies 4.68Hz, 9.86Hz)
	2Hz Low-pass Filter for Pitch Rate	5.0x	Stable
		5.5x(14.81dB)	Unstable (Critical state, instability frequency 3.80Hz)
		6.0x	Unstable (Instability frequency 3.80Hz)
BA03	No Filter	5.0x	Stable
		7.0x	Stable
		8.0x(18.06dB)	Slowly Unstable (Instability frequency 2.3Hz)
		8.5x(18.59dB)	Unstable (Instability frequency 3.80Hz)

TABLE 21. Items and parameters of lateral closed-loop test.

No.	Control Scheme	Altitude(m)	Control Gain
BB01	BTT	1500	K
BB02	BTT	20000	K
BB03	STT	1500	K

1) Closed-loop Impulse Response Test

The longitudinal closed-loop test consists of three sets of states with different control parameters, as shown in Table 19. In these sets, the longitudinal channel control gain gradually increases from the rated value to 2 times the gain (which can be increased by factors of 1.0, 1.5, and 2.0), while the lateral and heading channel control gains remain at their rated values. One of these states can be selected, and the gain multiplier can be further increased based on the results of the open-loop test to verify the reliability of the findings.

In the closed-loop impulse response test of the longitudinal channel, the BA02 state, with an excitation signal amplitude of 8 degrees and the smallest open-loop amplitude margin, underwent both filtered and unfiltered closed-loop impulse response tests. The key test results are summarized in Table 20. It is observed that BA01 and BA03 correspond to the 1500-meter low-altitude state of the BTT and STT control schemes, respectively, with an amplitude margin of approximately 18dB and an instability frequency of 3.8Hz, consistent with the open-loop frequency response test results. BA02 corresponds to the 15000-meter altitude state of the BTT control scheme, with an amplitude margin of less than

TABLE 22. Closed-loop impulse response test results (lateral channel).

No.	Filter	Control Gain	Stability
BB01	No Filter	2.0x	Stable
		4.0x(12.04dB)	Stable
		5.0x(13.98dB)	Unstable (Critical state)
BB02	No Filter	1.5x	Stable
		2.0x(6.02dB)	Unstable (Instability frequency 6.6Hz)
	2Hz Low-pass Filter for Roll Rate	2.0x	Stable
		6.0x	Stable
		9.0x(19.08dB)	Stable
BB03	No Filter	0.5x	Stable
		1.0x	Unstable (Instability frequency 6.6Hz)
	2Hz Low-pass Filter for Roll Rate	2.0x	Stable
		2.5x(7.96dB)	Stable
		3.0x(9.54dB)	Unstable (Instability frequency 6.35Hz)

TABLE 23. Items and parameters of heading closed-loop test.

No.	Control Scheme	Altitude(m)	Control Gain
BC01	BTT	1500	K
BC02	BTT	20000	K
BC03	STT	1500	K

8.0dB without a filter. However, after adding the filter, the amplitude margin increases to 14.8dB, with an instability frequency of 3.8Hz, slightly lower than the results of the open-loop frequency response test.

The transverse closed-loop test comprises three sets of states with different control parameters, as depicted in Table 21. In these sets, the transverse control gain gradually increases from the rated value to 2 times the gain (which can be incremented by factors of 1.0, 1.5, and 2.0 successively), while the longitudinal and heading channel control gains remain at their rated values. One of these states can be selected, and the gain multiplier can be further increased based on the results of the open-loop test to assess the reliability of the findings.

In the closed-loop impulse response test of the lateral channel, both filtered and unfiltered closed-loop impulse response tests were conducted for BB02 and the unstable BB03 state, with an excitation signal amplitude of 8 degrees. The key test results are presented in Table 22.

From the Table 22, it is evident that BB01 corresponds to the 1500-meter low-altitude state of the BTT control scheme, exhibiting a closed-loop amplitude margin of approximately 13dB, closely aligning with the open-loop frequency response test result (slightly higher amplitude margin than the open-loop result). BB02 corresponds to the 20000-meter high-altitude state of the BTT control scheme. After adding a 2Hz low-pass filter, the amplitude margin increased from less than 6dB to over 19dB. The instability frequency is 6.6Hz, demonstrating good agreement between the closed-loop and open-loop frequency response test results. BB03 corresponds to the 1500-meter low-altitude state of the STT control scheme. With the addition of a 2Hz low-pass filter, stability improved, and the amplitude margin

TABLE 24. The results of closed-loop impulse response test (Heading channel).

No.	Control Gain Multiplier	Stability
BC01	20x	Stable
BC02	20x	Stable
BC03	20x	Stable

TABLE 25. Stability results of KB03 state under three filter schemes.

No.	Filter	Amplitude Margin(dB)	Phase Margin (Deg)	Overall Margin (dB)	Stability
KB03	No Filter	-1.47(6.7Hz)	——	-5.78(6.9Hz)	Unstable
	Filter 1	11.65(6.1Hz)	——	4.45(6.9Hz)	Stable
	Filter 2	15.08(6.1Hz)	——	7.61(6.9Hz)	Stable
	Filter 3	17.74(5.8Hz)	——	5.23(6.9Hz)	Stable

increased to slightly less than 9.5dB from the unstable state, aligning closely with the open-loop frequency response test results (slightly lower amplitude margin than the open-loop results).

The heading closed-loop test comprises three sets of states according to different control parameters, as detailed in Table 23. In these states, the heading control gain gradually increases from the rated value to 2 times the gain (with increments of 1.0, 1.5, and 2.0), while the longitudinal and lateral channel control gains remain at their rated values. One of these states can be chosen to further increase the gain multiple based on the results of the open-loop tests, thereby verifying the reliability of the open-loop test results.

In the closed-loop impulse response test of the heading channel, with an excitation signal amplitude of 8 degrees, considering that the open-loop amplitude margin of the heading channel is not less than 40dB, the closed-loop test only considers states with a control gain multiple of 20 or 25. The test results are listed in Table 24, and all three groups of states exhibit extremely high stability.

B. FILTER DESIGN

To address the state with the lowest amplitude margin observed in both open and closed-loop tests (specifically, the KB03 lateral channel STT control scheme at 1500 meters low altitude), we considered the frequency response characteristics of angle and angular velocity loops obtained from open-loop frequency response tests without filters. Subsequently, we evaluated three filter schemes to compare their impact on the stability of the servoelasticity system.

The three filter schemes evaluated were as follows:

Filter 1: Angular velocity 2Hz low-pass filter

Filter 2: Angular velocity 2Hz low-pass filter + Angle 2Hz low-pass filter

Filter 3: Angular velocity 2Hz low-pass filter + Angular velocity structural notch filter

Parameters for the 2Hz low-pass filter (using a 40ms sampling period bilinear transform discrete):
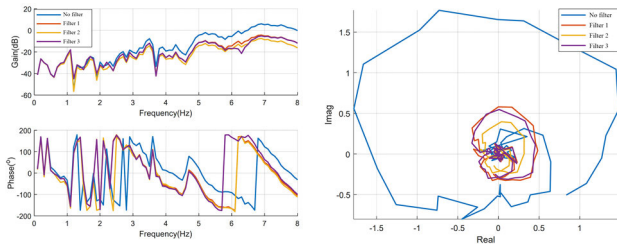
$$G_{LPF}(s) = \frac{12.5664}{s + 12.5664}$$

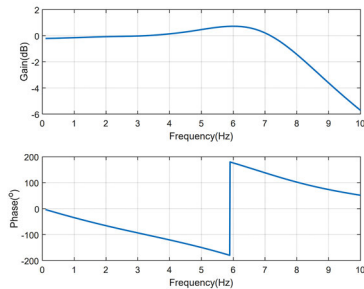**FIGURE 15.** Comparison of Bode/Nyquist plots for three filter schemes.

FIGURE 16. Amplitude-Frequency and Phase-Frequency Curves of the Rudder System Transfer Function.

$$G_{LPF}\left(z^{-1}\right) = \frac{0.2008 + 0.2008z^{-1}}{1 - 0.5983z^{-1}} \tag{28}$$

Parameters for the structural notch filter (using 40ms sampling period bilinear transform discrete):

$$G_{NF}(s) = \frac{s^2 + 1.0053s + 2526.6187}{s^2 + 8.0425s + 2526.6187}$$

$$G_{NF}\left(z^{-1}\right) = \frac{0.9352 + 0.009807z^{-1} + 0.9167z^{-2}}{1 + 0.009807z^{-1} + 0.8519z^{-2}} \tag{29}$$

The analysis results of servoelasticity stability for this state under the three filter schemes are listed in Table 25, and the corresponding open-loop frequency response Bode plots and Nyquist plots are shown in Figure 15. From the analysis results, it can be observed that the amplitude margin gradually increases from Filter 1 to Filter 3.

C. RUDDER SYSTEM TRANSFER FUNCTION FITTING

The fitted rudder system transfer function can be used for aeroservoelasticity theoretical analysis. To ensure conservative theoretical analysis results and higher safety margins, representative data with significant phase characteristics and a wide bandwidth from rudder system tests were selected for transfer function fitting. The KB01 lateral open-loop test data was utilized, with the aileron input signal as the input and the left outboard aileron feedback signal as the output, for a fourth-order transfer function fitting.

The fitted rudder system transfer function is expressed as follows:

$$G_a(s)$$
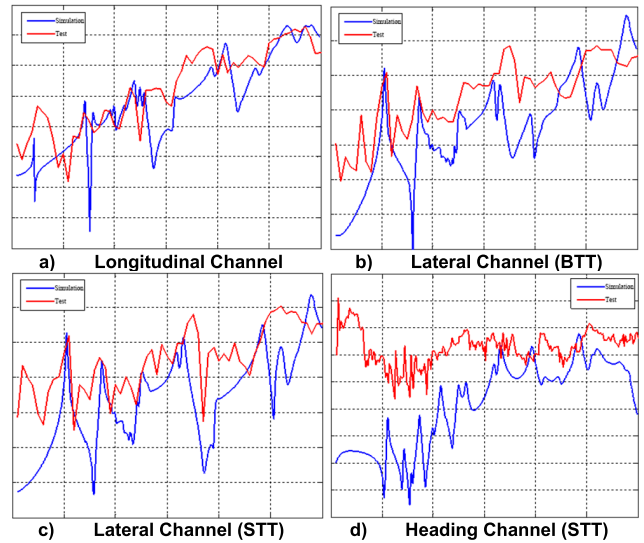$$= \frac{19.04s^3 - 1799.13s^2 + 87029.48s - 1036681.88}{s^4 + 29.67s^3 + 1561.92s^2 - 15277.32s - 1062126.23} \tag{30}$$

a) Longitudinal Channel   b) Lateral Channel (BTT)

c) Lateral Channel (STT)   d) Heading Channel (STT)

FIGURE 17. Ground servoelasticity Open-loop Transfer Function Amplitude-Frequency Curve.

TABLE 26. Parameters of analysis state.

No.	Altitude (m)	Atmospheric Density (kg/m3)	True Airspeed (m/s)
001	0	1.2250	10.69
002	1500	1.0581	11.50
003	5000	0.7364	13.79
004	10000	0.4127	18.42
005	15000	0.1937	26.88
006	20000	0.0880	39.89

Figure 16 shows the magnitude and phase frequency response curves of the aforementioned model. The bandwidth of this rudder system model is 8.72Hz (-3dB), with the rudder system reversing at 5.89Hz.

V. AEROSERVOELASTICITY SIMULATION
A. GROUND SERVOELASTICITY STABILITY ANALYSIS
On the basis of the modified finite element model of the UAV structure according to the modal test, the elastic stability analysis of the ground servo without considering aerodynamic forces is conducted initially. It is worth noting that the damping ratio of each natural mode is assumed to be 0.01 by default.

For the longitudinal channel KA02, the transverse channels KB02 (BTT) and KB02 (STT), as well as the heading channel KC03 (STT), typical states are selected, and a comparison between the simulation results and the experimental results is provided, as shown. The comparison demonstrates that the simulation results are largely consistent with the experimental findings.

B. AEROSERVOELASTICITY STABILITY ANALYSIS
There are six state points analyzed in this stage, with heights of 5 m, 1500 m, 5000 m, 10000 m, 15000 m, and 20000 m. The velocities are uniformly taken as those corresponding to
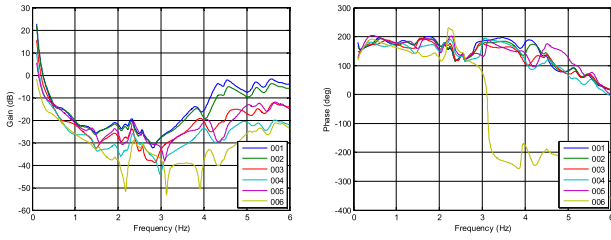
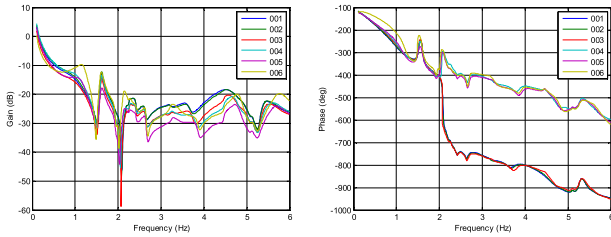**FIGURE 18.** Longitudinal Channel Aerodynamic Servoelastic System Open-loop Transfer Function (6 States).

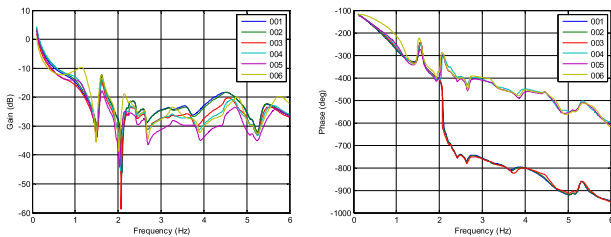**FIGURE 19.** Lateral Channel (BTT) Aerodynamic Servoelastic System Open-loop Transfer Function (6 States).

FIGURE 20. Lateral Channel (STT) Aerodynamic Servoelastic System Open-loop Transfer Function (6 States).
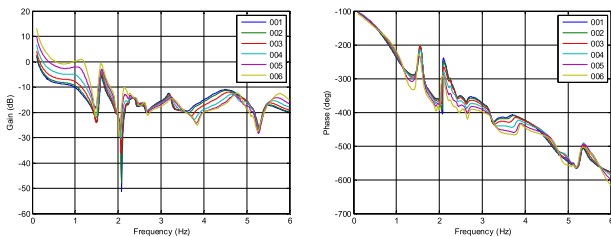

FIGURE 21. Heading Channel (STT) Aerodynamic Servoelastic System Open-loop Transfer Function (6 States).

a dynamic pressure of 70 Pa. For this purpose, the parameters of the analyzed states are listed in Table 26.

The analysis outcomes depicted in Figure 18 to Figure 21 reveal the following:

(1) The lateral channel (BTT) and heading channel (STT) for the six examined state points exhibit stability and possess a significant stability margin.

(2) The longitudinal channels for the six analyzed state points demonstrate stability; however, it is noteworthy that the open-loop transfer functions of the first and second state points manifest large amplitude values within the 4 to 6 Hz range, resulting in a diminished amplitude margin.

(3) The lateral channel (STT) for the six analyzed state points is stable; nevertheless, it should be highlighted that the amplitude of the open-loop transfer function within the 0.2 to 1.4 Hz range escalates with the vacuum velocity, leading to an amplitude margin below 6 dB for the 4th, 5th, and 6th state points.

It is essential to clarify that the aerodynamic characteristics utilized for this analysis phase were computed using the panel method, and no corrections were made based on wind tunnel test data for the overall aircraft or control surface aerodynamic characteristics.

VI. CONCLUSION

The presented study successfully conducted a comprehensive ground servoelasticity test on a high-aspect-ratio wing-layout UAV. Initially, corrective measures were applied to the suspension system to account for additional stiffness. Subsequently, modal testing of the entire aircraft was carried out, followed by open-loop frequency response testing and closed-loop impulse response testing, along with the design of appropriate filters.

The analysis of elastic stability on the ground, disregarding aerodynamic forces, was performed, and the simulation results were compared with experimental data. The key findings are summarized as follows:

The results of both the open-loop frequency response test and the closed-loop impulse response test exhibited a high level of agreement across all states. This mutual verification between open-loop and closed-loop tests underscores the reliability of the obtained results, indicating that they accurately reflect the servoelastic stability of the solar UAV under test conditions.

Each state of the longitudinal, transverse, and heading channels demonstrated stability after the implementation of suitable filters. Moreover, these systems met specification requirements, exhibiting an amplitude margin greater than 6 dB and a phase margin exceeding 45°.

The study has established a preliminary framework for the ground servoelasticity testing of super-large, flexible, low-frequency structures with wing layouts. This methodology lays a solid foundation for future investigations into high-aspect-ratio joined-wing aircraft, offering significant engineering applications.

Furthermore, it is acknowledged that large aspect ratio aircraft often involve certain nonlinear factors. Consequently, future research will expand upon the current study to explore aeroservoelasticity testing of ultra-large aspect ratio wing layout aircraft under nonlinear conditions, leveraging the insights gained from this foundational investigation.

DECLARATION OF COMPETING INTEREST

The authors declare that they have no known competing financial interests or personal relationships that could have appeared to influence the work reported in this paper.

REFERENCES

[1] C. He, F. Zhan, L. Ma, G. Chen, and J. Ma, "Aero-structural design of joined-wing aircraft based on high-fidelity model," *Chin. J. Aeronaut.*, vol. 37, no. 4, pp. 363–377, Apr. 2024, doi: 10.1016/j.cja.2023.10.029.

[2] Y. Hu, Y. Yang, X. Ma, and S. Li, "Computational optimal launching control for balloon-borne solar-powered unmanned aerial vehicles in near-space," *Sci. Prog.*, vol. 103, no. 1, Jan. 2020, Art. no. 003685041987775.

[3] W. Youn, H. Choi, A. Cho, S. Kim, and M. B. Rhudy, "Accelerometer fault-tolerant model-aided state estimation for high-altitude long-endurance UAV," *IEEE Trans. Instrum. Meas.*, vol. 69, no. 10, pp. 8539–8553, Oct. 2020.

[4] R. Cavallaro and L. Demasi, "Challenges, ideas, and innovations of joined-wing configurations: A concept from the past, an opportunity for the future," *Prog. Aerosp. Sci.*, vol. 87, pp. 1–93, Nov. 2016.

[5] E. Reichenbach, "Aeroservoelastic design and test validation of the joined wing sensorcraft," in *Proc. 26th AIAA Appl. Aerodyn. Conf.* Honolulu, HI, USA: American Institute of Aeronautics and Astronautics, Aug. 2008, doi: 10.2514/6.2008-7189.

[6] T. Aarons, R. Canfield, C. Woolsey, J. Richards, A. Suleman, N. Lindsley, and M. Blair, "Design for flight test of a scaled joined wing SensorCraft," in *Proc. 52nd AIAA/ASME/ASCE/AHS/ASC Struct., Struct. Dyn. Mater. Conf.* Denver, CO, USA: American Institute of Aeronautics and Astronautics, Apr. 2011, doi: 10.2514/6.2011-2011.

[7] E. Reichenbach and V. Sharma, "Development of an innovative support system for SensorCraft model," in *Proc. 52nd AIAA/ASME/ASCE/AHS/ASC Struct., Struct. Dyn. Mater. Conf.* Denver, CO, USA: American Institute of Aeronautics and Astronautics, Apr. 2011, doi: 10.2514/6.2011-1958.

[8] J. Heeg and E. Morelli, "Evaluation of simultaneous multisine excitation of the joined wing aeroelastic wind tunnel model," in *Proc. 52nd AIAA/ASME/ASCE/AHS/ASC Struct., Struct. Dyn. Mater. Conf.* Denver, CO, USA: American Institute of Aeronautics and Astronautics, Apr. 2011, doi: 10.2514/6.2011-1959.

[9] E. Reichenbach, M. Castelluccio, and B. Sexton, "Joined wing sensorcraft aeroservoelastic wind tunnel test program," in *Proc. 52nd AIAA/ASME/ASCE/AHS/ASC Struct., Struct. Dyn. Mater. Conf.* Denver, CO, USA: American Institute of Aeronautics and Astronautics, Apr. 2011, doi: 10.2514/6.2011-1956.

[10] M. Scott, A. Enke, and J. Flanagan, "SensorCraft free-flying aeroservoelastic model: Design and fabrication," in *Proc. 52nd AIAA/ASME/ASCE/AHS/ASC Struct., Struct. Dyn. Mater. Conf.* Denver, CO, USA: American Institute of Aeronautics and Astronautics, Apr. 2011, doi: 10.2514/6.2011-1957.

[11] J. Richards, J. S. Garnand-Royo, A. Suleman, R. A. Canfield, and C. A. Woolsey, "Design and evaluation of aeroelastically tuned joined-wing SensorCraft flight test article," in *Proc. 54th AIAA/ASME/ASCE/AHS/ASC Struct., Struct. Dyn., Mater. Conf.* Boston, MA, USA: American Institute of Aeronautics and Astronautics, Apr. 2013, doi: 10.2514/6.2013-1786.

[12] F. Kimler and R. Canfield, "Structural design of wing twist for pitch control of joined wing SensorCraft," in *Proc. 11th AIAA/ISSMO Multidisciplinary Anal. Optim. Conf.* Portsmouth, VA, USA: American Institute of Aeronautics and Astronautics, Sep. 2006, doi: 10.2514/6.2006-7134.

[13] R. Scott, D. Coulson, M. Castelluccio, and J. Heeg, "Aeroservoelastic wind-tunnel tests of a free-flying, joined-wing SensorCraft model for gust load alleviation," in *Proc. 52nd AIAA/ASME/ASCE/AHS/ASC Struct., Struct. Dyn. Mater. Conf.* Denver, CO, USA: American Institute of Aeronautics and Astronautics, Apr. 2011, doi: 10.2514/6.2011-1960.

[14] J. Grauer, J. Heeg, and E. Morelli, "Real-time frequency response estimation using joined-wing SensorCraft aeroelastic wind-tunnel data," in *Proc. AIAA Atmos. Flight Mech. Conf.* Minneapolis, MN, USA: American Institute of Aeronautics and Astronautics, Aug. 2012, doi: 10.2514/6.2012-4641.

[15] V. E. L. Gasparetto, M. Machado, and S. H. S. Carneiro, "Experimental modal analysis of an aircraft wing prototype for SAE aerodesign competition," *DYNA*, vol. 87, no. 214, pp. 100–110, Jul. 2020.

[16] Y. Liu and C. Xie, "Aeroservoelastic stability analysis for flexible aircraft based on a nonlinear coupled dynamic model," *Chin. J. Aeronaut.*, vol. 31, no. 12, pp. 2185–2198, Dec. 2018, doi: 10.1016/j.cja.2018.08.019.

[17] Z. Zhang, Y. Yang, S. Ricci, A. D. Gaspari, C. Song, and C. Yang, "Aeroservoelastic optimization of a high aspect transport wing with morphing trailing edge," in *Proc. 32nd Congr. Int. Council Aeronaut. Sci.*, 2021, pp. 1–11.

[18] R. Huang, X. Yu, and X. Zhou, "Efficient nonlinear aeroservoelastic modeling for morphing wing with bilinear stiffness," *AIAA J.*, vol. 60, no. 5, pp. 3135–3146, May 2022, doi: 10.2514/1.j060923.

[19] O. D. Dantsker, M. Caccamo, M. Vahora, and R. Mancuso, "Flight & ground testing data set for an unmanned aircraft: Great planes avistar elite," in *Proc. AIAA Scitech Forum*, 2020, p. 0780.

[20] P. A. Bońkowski, P. Bobra, Z. Zembaty, and B. Jędraszak, "Application of rotation rate sensors in modal and vibration analyses of reinforced concrete beams," *Sensors*, vol. 20, no. 17, p. 4711, Aug. 2020.

BI YING received the Ph.D. degree in aircraft design from Beihang University, in 2017. She is currently an Assistant Researcher with the Institute of Engineering Thermophysics, Chinese Academy of Sciences. Her research interests include aeroelasticity, gust responses, gust alleviation, and active control.

YING ZHUOLIN received the bachelor's degree in mechanical engineering from Nanjing University of Aeronautics and Astronautics, in 2022. He is currently pursuing the Ph.D. degree with the Institute of Engineering Thermophysics, Chinese Academy of Science, Beijing, China. His research interests include aero-servoelasticity, nonlinear dynamics analysis, gust alleviation, and active control.

ZHU ZIJIAN received the bachelor's degree in energy and power engineering from Tianjin University, in 2021. He is currently pursuing the Ph.D. degree with the Institute of Engineering Thermophysics, Chinese Academy of Science, Beijing, China. His research interests include UAV structural designs, nonlinear dynamics modeling, and aeroelastic characteristics analysis.

ZHU CHEN received the bachelor's degree in mechanical engineering from the University of Shanghai for Science and Technology, in 2022. He is currently pursuing the Ph.D. degree with the Institute of Engineering Thermophysics, Chinese Academy of Science, Beijing, China. His research interests include UAV structural designs and nonlinear aeroelastic characteristics analysis of unmanned multi-body aircraft.

• • •